Received August 14, 2019, accepted August 30, 2019, date of publication September 11, 2019,
date of current version September 24, 2019.

Digital Object Identifier 10.1109/ACCESS.2019.2940283

High-Precision Imaging Algorithm for Highly Squinted SAR With 3D Acceleration

BANG HUANG[1], (Student Member, IEEE), SHUNSHENG ZHANG[2], WEN-QIN WANG[1], (Senior Member, IEEE), TIANXING LIAO[1], XIN ZHAO[3], AND DUNWEI DU[3]

[1]School of Information and Communication Engineering, University of Electronic Science and Technology of China, Chengdu 611731, China
[2]Research Institute of Electronic Science and Technology, University of Electronic Science and Technology of China, Chengdu 611731, China
[3]Beijing Institute of Mechanical and Electrical Engineering, Beijing 100094, China

Corresponding author: Shunsheng Zhang (zhangss@uestc.edu.cn)

This work was supported by the National Natural Science Foundation of China (NSFC) under Grant 61571081 and Grant 61671122.

ABSTRACT In conventional synthetic aperture radar (SAR) processing algorithms, it is generally assumed that the platform performs a uniform linear motion. However, if there is a three-dimensional acceleration during the flight, the motion trajectory will greatly increase the image processing complexity, especially in highly squinted scenarios. This paper proposes a high-precision imaging algorithm for highly squinted SAR with 3D acceleration. Firstly, the range history is extended by the Taylor series, and then a two-dimensional non-uniform fast Fourier transform (2D-NUFFT) is presented to focus the SAR image in range velocity domain. Moreover, as terrain matching is required in practice, the range-velocity image is further transformed into range-azimuth domain. The effectiveness of the proposed algorithm for highly squinted SAR imaging is verified with both simulation data for multi-point targets and experimental data for surface targets.

INDEX TERMS 3D acceleration, highly squinted, high-precision imaging, nonuniform fast Fourier transform, NUFFT, 2D-NUFFT, synthetic aperture radar, SAR.

I. INTRODUCTION

Although synthetic aperture radar (SAR) has received much recognition in recent year, high-precision imaging algorithm for highly squinted SAR with 3D acceleration still has not been well handled in the literature. Although the range-azimuth coupling highly squinted SAR can be handled by the range cell migration correction (RCMC) [1], [2] algorithm, the inherent range-dependent squinted angle and acceleration will make the range cell migration (RCM) to vary along with the flight track. This spatial variation will lead to serious phase errors and consequently, the imaging performance will be seriously degraded if no additional compensations are applied.

Imaging algorithm for highly squinted SAR has been discussed in several papers [3]–[5]. The polar coordinate format algorithm (PFA) compensates the highly squinted SAR data to the line of sight (LOS) direction, so that the range offset for any oblique view can be easily compensated [3], but it approximates the actual spherical wavefront as a planar. A digital concentrating preprocessing method based on the 2-step PFA method was proposed in [4] and an improved range-Doppler algorithm (RDA) was proposed in [6] to deal with the problems caused by highly squinted angle and large velocity but without considering acceleration. A 3D motion compensation (MOCO) algorithm was proposed in [7], but it can't compensate the errors well with highly squinted angle. By the employment of motion compensation [7], a modified nonlinear chirp scaling (MNLCS) was adopted in [5] to handle the 3D acceleration problems, while it has a limited scope of application. Lu *et al.* [8] proposed a multi-antenna approach for the forward-looking high-resolution SAR imaging under the curve trajectory. Liu *et al.* [9] analyzed the error of the nonlinear trajectory.

Although the omega-K algorithm [10] is the widely preferred method for accelerated SAR [11]–[13], there are some difficulties in applying the omega-K algorithm without modification for the highly squinted SAR with 3D acceleration. One is how to get an accurate analytical spectrum. In the presence of acceleration, the samples in the azimuth wavenumber domain will be nonuniform and classic Fourier transform (FT) cannot be applied. Tang *et al.* [14], [15]

The associate editor coordinating the review of this manuscript and approving it for publication was Bora Onat.

has put forward an omega-K algorithm for highly squinted SAR with constant acceleration. Nevertheless, the assumed acceleration is relatively small and only two-dimensional acceleration is considered. Another problem is the process of linearizing the frequency in the two-dimensional spectrum must be multiplied by a reference function which cannot be easily obtained.

In the case of the highly squinted angle in [16]–[19], the original range formula is modified based on the RCM algorithm, and some new algorithms are proposed. However, the imaging accuracy is not high, or the acceleration is not considered, or the computational complexity is high. Therefore, [20] proposed a range perturbation approach (RPA) for highly squinted SAR with nonlinear trajectory on the basis of the above papers. [21]–[23] has put forward algorithm of nonuniform fast Fourier transforms (NUFFT's) for SAR, but they don't consider the complex case of track of the platform flight.

In this paper, we propose a high-precision imaging algorithm for highly squinted SAR with 3D acceleration. We formulate the range history through Taylor series expansion to avoid the use of series reversion [24] and derive a new two-dimensional (2D) spectra model for the SAR data that can be easily focused by NUFFT, followed by the slant range to ground range conversion [25].

This paper is extended version of [26]. The remaining sections of this paper are organized as follows: The signal model for the highly squinted SAR with 3D acceleration is presented in Section II, followed by the proposed 2D spectra model in Section III. Next, the 2D-NUFFT-based imaging algorithm and the slant range to ground range conversion are derived in Section IV. Finally, image formulation processing results and conclusion are provided in Sections V and VI, respectively.

II. SIGNAL MODEL FOR HIGHLY SQUINTED SAR

Figure.1 illustrates the imaging geometry for the highly squinted SAR with 3D acceleration. the location vector of the radar platform moves with a general velocity $\boldsymbol{V}$ and a highly acceleration vector $\boldsymbol{A}$. The origin O is the projection of the antenna phase center and θ is the squint angle. The platform location vector $\boldsymbol{P}(u)$ can be expressed as

$$\boldsymbol{P}(u) = \boldsymbol{P_0} + \boldsymbol{V}u + \frac{1}{2}\boldsymbol{A}u^2 \tag{1}$$

where $\boldsymbol{P_0}$ is the initial SAR platform location vector. u is the azimuth slow time. The instantaneous range between radar platform and the point target D is then represented by

$$\begin{aligned} R(u;\boldsymbol{s}) &= \|\boldsymbol{P}(\boldsymbol{u}) - \boldsymbol{s}\|_2 \\ &= \left[\left(\boldsymbol{P_0} + \boldsymbol{V}u + \frac{1}{2}\boldsymbol{A}u^2 - \boldsymbol{s}\right)^T (\boldsymbol{P_0} \right. \\ &\qquad \left. + \boldsymbol{V}u + \frac{1}{2}\boldsymbol{A}u^2 - \boldsymbol{s})\right]^{1/2} \end{aligned} \tag{2}$$

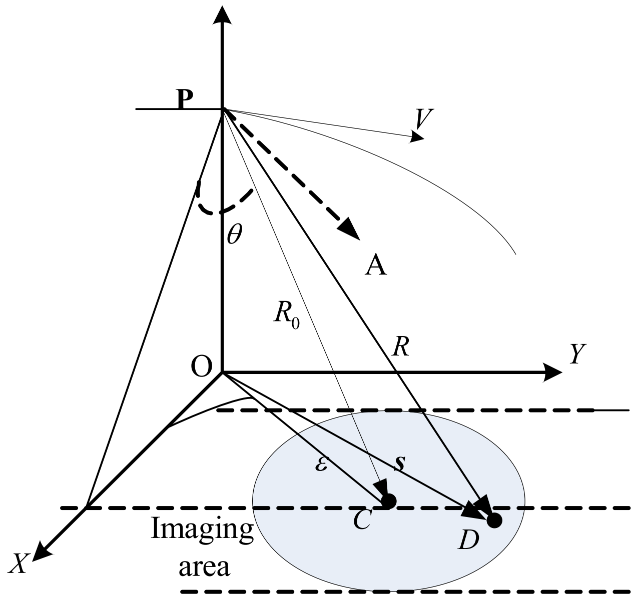

FIGURE 1. Geometric model for high-precision imaging.

where $\boldsymbol{s}$ is the vector from origin O to the target D, whose expression is $\boldsymbol{s} = [x_s, y_s, z_s]^T$. (2) can be further rewritten as

$$\begin{aligned} R(u;\boldsymbol{s}) = \Big[&\|\boldsymbol{P_0} - \boldsymbol{s}\|_2^2 + 2(\boldsymbol{P_0} - \boldsymbol{s})^T \boldsymbol{V}u + \|\boldsymbol{V}\|_2^2 u^2 \\ &+ (\boldsymbol{P_0} - \boldsymbol{s})^T \boldsymbol{A}u^2 + \boldsymbol{V}^T\boldsymbol{A}u^3 + \frac{1}{4}\|\boldsymbol{A}\|_2^2 u^4 \Big]^{1/2} \end{aligned} \tag{3}$$

It can be expanded into series with respect to the azimuth time:

$$R(u;\boldsymbol{s}) = \sum_{n=0}^{+\infty} \frac{1}{n!} k_n(\boldsymbol{s}) u^n \tag{4}$$

where $k_n(\boldsymbol{s})$ is represented by

$$k_n(\boldsymbol{s}) = \left. \frac{d^n R(u;\boldsymbol{s})}{du^n} \right|_{u=0} \tag{5}$$

For the first five terms, we can get

$$k_0(\boldsymbol{s}) = \|\boldsymbol{P_0} - \boldsymbol{s}\|_2 \tag{6}$$

$$k_1(\boldsymbol{s}) = \frac{\langle(\boldsymbol{P_0} - \boldsymbol{s}), \boldsymbol{V}\rangle}{k_0(\boldsymbol{s})} \tag{7}$$

$$k_2(\boldsymbol{s}) = \frac{\|\boldsymbol{V}\|_2^2 + \langle(\boldsymbol{P_0} - \boldsymbol{s}), \boldsymbol{A}\rangle - k_1(\boldsymbol{s})}{k_0(\boldsymbol{s})} \tag{8}$$

$$k_3(\boldsymbol{s}) = \frac{\langle\boldsymbol{V}, \boldsymbol{A}\rangle - 3k_1(\boldsymbol{s})\, k_2(\boldsymbol{s})}{k_0(\boldsymbol{s})} \tag{9}$$

$$k_4(\boldsymbol{s}) = \frac{3\|\boldsymbol{A}\|_2^2 - 4k_1(\boldsymbol{s})\, k_3(\boldsymbol{s}) - 3{k_1}^2(\boldsymbol{s})}{k_0(\boldsymbol{s})} \tag{10}$$

where $\langle\cdot\rangle$ is the inner product operator and $\|\cdot\|_2^2$ is the 2-norm operator.

For a point target, the received baseband signal can be expressed as

$$Ss(t, u; \boldsymbol{s}) = \sigma(\boldsymbol{s})\, g\left[t - \frac{2R(u;\boldsymbol{s})}{c}\right] \times \exp\left[-j2\pi f_c \frac{2R(u;\boldsymbol{s})}{c}\right] \times \exp\left\{j\pi K\left[t - \frac{2R(u;\boldsymbol{s})}{c}\right]^2\right\} \quad (11)$$

where K is the frequency modulation rate. t stands for the fast time in range domain. $g(t)$ represents the baseband waveform. $\sigma(\boldsymbol{s})$ is the target reflection coefficient. f_c is the carrier frequency and c is the speed of light.

According to the stationary phase (SP) principle, the Fourier transform of (12) will yield

$$\begin{aligned} Ss(f_t, u; \boldsymbol{s}) &= \int Ss(t, u; \boldsymbol{s}) \exp(-j2\pi f_t t) dt \\ &= \sigma(\boldsymbol{s})\, G\left[\frac{f_t}{K}\right] \exp\left(-j\pi \frac{f_t^{\,2}}{K}\right) \\ &\quad \times \exp\left[-j2\pi(f_c + f_t)\frac{2R(u;\boldsymbol{s})}{c}\right] \end{aligned} \quad (12)$$

where, f_t is the frequency in range domain, $G\left[\frac{f_t}{K}\right]$ is the spectrum of the transmitted signal. Without loss of generality, we are assuming that

$$\left\| G\left(\frac{f_t}{K}\right)\right\|_2^2 \equiv 1, \quad \forall f_t \in [-0.5B, +0.5B] \quad (13)$$

with B being the transmitted signal bandwidth.

III. 2D SPECTRA MODEL FOR HIGHLY SQUINTED SAR WITH 3D ACCELERATION

A. 2D SPECTRA MODEL

No accelerations are considered in above analysis. However, for the highly squinted SAR with 3D acceleration, more accurate spectra is needed. More seriously, the 3D acceleration makes the azimuth sampling signal being non-uniform and consequently, classic fast Fourier transform (FFT) cannot be directly applied. Moreover, the spatial variance problem should be well handled. To resolve these problems, we develop an approximated range history model, so that the 2D-NUFFT algorithm [27]–[30] can be adopted for subsequent processing.

For the target #C located at the scene center, its range history can be expressed as

$$\begin{aligned} R_0(u;\boldsymbol{\varepsilon}) &= \|\boldsymbol{P}(\boldsymbol{u}) - \boldsymbol{\varepsilon}\|_2 \\ &= \left[\left(\boldsymbol{P}_0 + \boldsymbol{V}u + \frac{1}{2}\boldsymbol{A}u^2 - \boldsymbol{\varepsilon}\right)^T (\boldsymbol{P}_0 + \boldsymbol{V}u + \frac{1}{2}\boldsymbol{A}u^2 - \boldsymbol{\varepsilon})\right]^{1/2} \end{aligned} \quad (14)$$

where $\boldsymbol{\varepsilon}$ is the vector from origin O to the central reference point (CRP), whose expression is $\boldsymbol{\varepsilon} = [x_\varepsilon, y_\varepsilon, z_\varepsilon]^T$.

The echo signal of center reference point after FFT at range dimension can be expressed as

$$Ss(f_t, u; \boldsymbol{\varepsilon}) = \sigma(\boldsymbol{\varepsilon}) \exp\left(-j\pi\frac{f_t^{\,2}}{K}\right) \times \exp\left(-j2\pi(f_c + f_t)\frac{2R_0(u;\boldsymbol{\varepsilon})}{c}\right) \quad (15)$$

Multiplying by the reference function yields

$$\begin{aligned} Ss_{\mathrm{RFM}}(f, u; \boldsymbol{s}) &= Ss(f, u; \boldsymbol{s}) \cdot Ss^*(f, u; \boldsymbol{\varepsilon}) \\ &= \sigma(\boldsymbol{\varepsilon})\,\sigma(\boldsymbol{s}) \exp\left[-j2\pi\,(f_c + f_t)\frac{2\Delta R(u;\boldsymbol{s})}{c}\right] \end{aligned} \quad (16)$$

According to (11) and (14), we can get the range expression for the center of the scene. Accordingly, the range histories for target #D and target #C can be obtained. In doing so, we can get

$$\begin{aligned} \Delta R(u;\boldsymbol{s}) &= R(u;\boldsymbol{s}) - R_0(u;\boldsymbol{\varepsilon}) \\ &= \Delta k_0(\boldsymbol{s}) + \Delta k_1(\boldsymbol{s})\, u + \sum_{n=2}^{+\infty} \Delta k_n(\boldsymbol{s})\, u^n \end{aligned} \quad (17)$$

According to the multivariate Taylor formula, $\Delta k_n(\boldsymbol{s})$ can be expressed as

$$\Delta k_n(\boldsymbol{s}) \approx \alpha_n \Delta k_0(\boldsymbol{s}) + \beta_n \Delta k_1(\boldsymbol{s}) \quad (18)$$

where α_n and β_n can be solved as follows

$$\alpha_n = \frac{\partial \Delta k_n(\boldsymbol{s})}{\partial \Delta k_0(\boldsymbol{s})} \quad (19)$$

$$\beta_n = \frac{\partial \Delta k_n(\boldsymbol{s})}{\partial \Delta k_1(\boldsymbol{s})} \quad (20)$$

That is

$$\alpha_n = \left[\frac{\frac{\partial k_n(\boldsymbol{s})}{\partial x}\frac{\partial k_0(\boldsymbol{s})}{\partial y} - \frac{\partial k_0(\boldsymbol{s})}{\partial x}\frac{\partial k_n(\boldsymbol{s})}{\partial y}}{\frac{\partial k_0(\boldsymbol{s})}{\partial x}\frac{\partial k_1(\boldsymbol{s})}{\partial y} - \frac{\partial k_1(\boldsymbol{s})}{\partial x}\frac{\partial k_0(\boldsymbol{s})}{\partial y}}\right] \quad (21)$$

$$\beta_n = \left[\frac{\frac{\partial k_0(\boldsymbol{s})}{\partial x}\frac{\partial k_n(\boldsymbol{s})}{\partial y} - \frac{\partial k_n(\boldsymbol{s})}{\partial x}\frac{\partial k_0(\boldsymbol{s})}{\partial y}}{\frac{\partial k_0(\boldsymbol{s})}{\partial x}\frac{\partial k_1(\boldsymbol{s})}{\partial y} - \frac{\partial k_1(\boldsymbol{s})}{\partial x}\frac{\partial k_0(\boldsymbol{s})}{\partial y}}\right] \quad (22)$$

Therefore, Eq.(18) can be further approximated as

$$\Delta R_{app}(u;\boldsymbol{s}) = \left[1 + \sum_{n=2}^{+\infty}\alpha_n u^n\right]\Delta k_0(\boldsymbol{s}) + \left[u + \sum_{n=2}^{+\infty}\beta_n u^n\right]\Delta k_1(\boldsymbol{s}) \quad (23)$$

Eq.(16) can be rewritten as

$$\begin{aligned} &Ss_{\mathrm{RFM}}(f_t, u; \boldsymbol{s}) \\ &= A(\boldsymbol{\varepsilon}, \boldsymbol{s}) \exp\left\{-j4\pi\,(f_c + f_t)\left[\frac{\left(1 + \sum_{n=2}^{+\infty}\alpha_n u^n\right)\Delta k_0(\boldsymbol{s})}{c} + \frac{\left(u + \sum_{n=2}^{+\infty}\beta_n u^n\right)\Delta k_1(\boldsymbol{s})}{c}\right]\right\} \end{aligned} \quad (24)$$

where $A(\boldsymbol{\varepsilon},s) = \sigma(\varepsilon)\,\sigma(\boldsymbol{s})$.

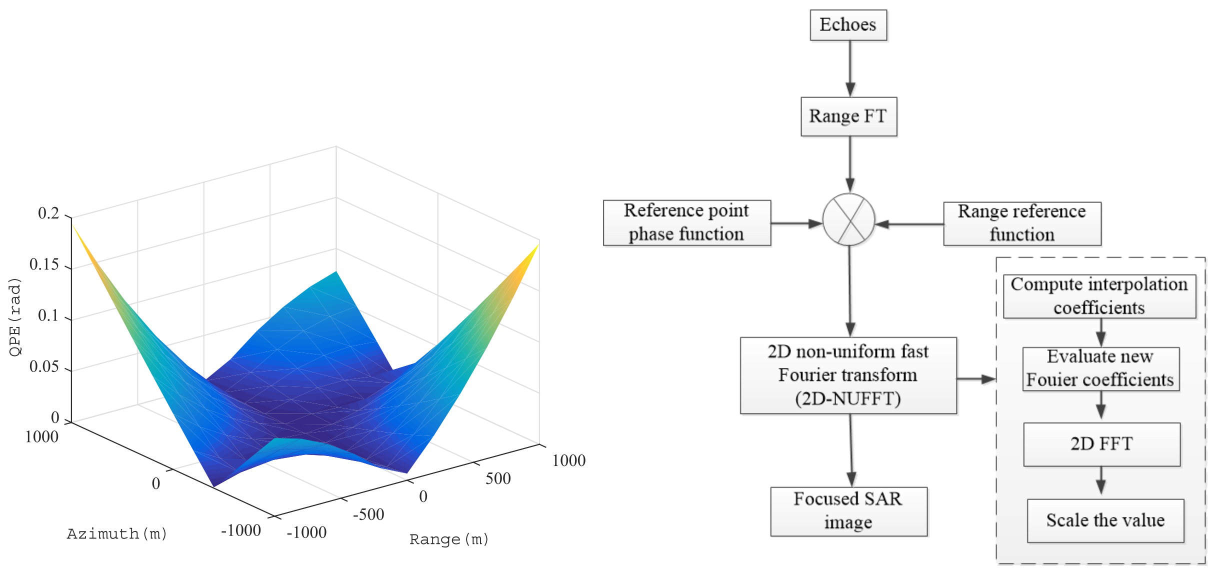

(a) (b)

FIGURE 2. (a) Quadratic Phase Error(QPE). (b) Flowchart of the imaging algorithm.

Defining

$$h_0(f_t, u) = \frac{2(f_c + f_t)}{c}\left[1 + \sum_{n=3}^{+\infty} \alpha_n u^n\right] - 2\frac{f_c}{c} \quad (25)$$

$$h_1(f_t, u) = \frac{2(f_c + f_t)}{c}\left[u + \sum_{n=2}^{+\infty} \beta_n u^n\right] \quad (26)$$

we can rewrite (24) as

$$\begin{aligned} Ss_{\text{RFM}}(h_0, h_1; \boldsymbol{s}) = A(\boldsymbol{\varepsilon}, \boldsymbol{s}) \exp\left[-j4\pi \frac{f_c \Delta k_0(\boldsymbol{s})}{c}\right] \\ \times \exp\left[-j2\pi h_0(f_t, u)\Delta k_0(\boldsymbol{s})\right. \\ \left.-j2\pi h_1(f_t, u)\Delta k_1(\boldsymbol{s})\right] \end{aligned} \quad (27)$$

B. MODEL ERROR ANALYSIS

From (18) and (23), we can get the approximation error:

$$\begin{aligned} e_R &= \Delta R(u; \boldsymbol{s}) - \Delta R_{app}(u; \boldsymbol{s}) \\ &= \sum_{n=2}^{+\infty} \Delta k_n u^n - \sum_{n=2}^{N} (\alpha_n \Delta k_0 + \beta_n \Delta k_1) u^n \end{aligned} \quad (28)$$

It can be reformulated as

$$\chi_R = \frac{2\pi}{\lambda}\left|\sum_{n=2}^{+\infty} \Delta k_n - \sum_{n=2}^{N} (\alpha_n \Delta k_0 + \beta_n \Delta k_1)\right|\left(\frac{T_s}{2}\right)^n \quad (29)$$

where the quadratic phase error is

$$\chi_{R,QPE} = \frac{2\pi}{\lambda}\left|\alpha_2 \Delta k_0 + \beta_2 \Delta k_1 - \Delta k_2\right|\left(\frac{T_s}{2}\right)^2 \quad (30)$$

which should be less than $\pi/4$ for high-precision imaging. Figure 2(a) is the quadratic phase error, which shows that the maximum phase error is 0.19 radians which is much smaller than the required value when the scene size is 2000m×2000m. It is indicated that the approximation error is ignorable now for SAR imaging in this case.

IV. 2D-NUFFT-BASED IMAGING ALGORITHM

A. 2D-NUFFT ALGORITHM

After the range history approximation, we develop a 2D-NUFFT-based imaging algorithm for the highly squinted SAR with 3D acceleration, which processing flow is illustrated in Figure 2(b).

Applying 2D-NUFFT to (27) yields

$$\begin{aligned} I(\Delta k_0(\boldsymbol{s}), \Delta k_1(\boldsymbol{s})) = A(\xi, \boldsymbol{s}) \iint S_{RFM}(f_t, u; \boldsymbol{s}) \\ \times \exp\left[j2\pi h_0(f_t, u)\Delta k_0(\boldsymbol{s})\right. \\ \left.+j2\pi h_1(f_t, u)\Delta k_1(\boldsymbol{s})\right] df_t du \end{aligned} \quad (31)$$

Assuming Δf_t and Δu are the sampled frequency intervals in the range and azimuth dimensions, respectively. While Δk_0 and Δk_1 are the sampled intervals for the slant range and flight speeds, respectively. According to the binary integral criteria, (31) can be modified to

$$I_{r,v} = \sum_{m=0}^{M-1}\sum_{n=0}^{N-1} B_{m,n} \exp\left(j\frac{2\pi}{M} x_r \gamma_{m,n} + j\frac{2\pi}{N} y_v \eta_{m,n}\right) \quad (32)$$

where $\Delta k_0, \Delta k_1 \in [0, 1]$,

$$\gamma_{m,n} = \frac{M}{\Delta h_0}\left[h_0(m \times \Delta f, n \times u) - h_{0c}\right] \quad (33)$$

$$\eta_{m,n} = \frac{N}{\Delta h_1}\left[h_1(m \times \Delta f, n \times \Delta u) - h_{1c}\right] \quad (34)$$

and $B_{m,n}$ is

$$B_{m,n} = S_{RFM}(r \times \Delta h_0, v \times \Delta h_1; s)\, \Delta f_t \Delta u A(\boldsymbol{\varepsilon})\pi \quad (35)$$

with $-\frac{M}{2} \leq r < \frac{M}{2}, -\frac{N}{2} \leq v < \frac{N}{2}$. M and N denote the sampling number in the range and azimuth dimensions, respectively, Δf_t and Δh_0, Δu and Δh_1 denote the sampling interval of original and new range frequency and azimuth time, while h_{0c} and h_{1c} are the midpoint of the irregular range frequency and azimuth time in the new transform domain.

Analogous to [26]–[30], we approximate the complex exponential terms of (27) by linear interpolation. In doing so, we then have

$$\exp\left(j\frac{2\pi}{M}x_r\gamma\right) = \frac{1}{a_r}\sum_{q=-Q}^{Q} c_q(\gamma)\exp\left\{j\frac{2\pi}{GM}r \cdot [round\,(G\gamma)+q]\right\} \quad (36)$$

$$\exp\left(j\frac{2\pi}{N}y_v\eta\right) = \frac{1}{b_v}\sum_{p=-Q}^{Q} d_p(\eta)\exp\left\{j\frac{2\pi}{GN}v \cdot [round\,(G\eta)+p]\right\} \quad (37)$$

where c_q and d_p are the interpolation coefficient with interpolation kernel length $2Q+1$. G stands for the interpolation factor. a_r and b_v are defined as the accuracy factor which are expressed as

$$a_r = \cos\left(\frac{\pi r}{GM}\right) \quad (38)$$

$$b_v = \cos\left(\frac{\pi v}{GN}\right) \quad (39)$$

Rewriting (36) in a vector as

$$\boldsymbol{A}(\gamma)\boldsymbol{c}(\gamma) = \boldsymbol{b}(\gamma) \quad (40)$$

where $\boldsymbol{A}(\gamma) = \left\{A(\gamma)_{i,j}\right\}$. Thus, we can get,

$$A(\gamma)_{i,j} = \exp\{j\frac{2\pi}{GM}\left(-\frac{M}{2}+i-1\right)[round\,(G\gamma) - Q + j - 1]\}, \quad 1 \leqslant i,\ j \leqslant 2Q+1 \quad (41)$$

$$\boldsymbol{c}(\gamma) = \left[c_{-Q}(\gamma), c_{-Q+1}(\gamma), \cdots, c_Q(\gamma)\right]^T \quad (42)$$

$$\boldsymbol{b}(\gamma) = \begin{bmatrix} a_{-\frac{M}{2}}\exp\left[j\frac{2\pi}{M}\left(-\frac{M}{2}\right)\gamma\right] \\ a_{-\frac{M}{2}+1}\exp\left[j\frac{2\pi}{M}\left(-\frac{M}{2}+1\right)\gamma\right] \\ \vdots \\ a_{\frac{M}{2}-1}\exp\left[j\frac{2\pi}{M}\left(\frac{M}{2}-1\right)\gamma\right] \end{bmatrix} \quad (43)$$

Usually $2Q+1 \ll M$, (40) is resolved as [31]

$$\mathbf{c}(\gamma) = \left(\boldsymbol{A}^H(\gamma)\boldsymbol{A}(\gamma)\right)^{-1}\boldsymbol{A}^H(\gamma)\boldsymbol{b}(\gamma) \quad (44)$$

where $\boldsymbol{A}^H(\gamma)$ is the complex conjugate transpose.

In order to facilitate the subsequent derivations, we define

$$\boldsymbol{E}(\gamma) = \boldsymbol{A}^H(\gamma)\boldsymbol{A}(\gamma) \quad (45)$$

$$\boldsymbol{d}(\gamma) = \boldsymbol{A}^H(\gamma)\boldsymbol{b}(\gamma) \quad (46)$$

where

$$E_{i,j} = \sum_{k=-\frac{M}{2}}^{\frac{M}{2}-1}\exp\left[j2\pi r\left(-\frac{i-j}{GM}\right)\right] = \begin{cases} \mathrm{M} & i=j \\ \exp\left[-j\pi\left(-\frac{i-j}{GM}\right)\right]\dfrac{\sin\left[\pi M\left(-\frac{i-j}{GM}\right)\right]}{\sin\left[\pi\left(-\frac{i-j}{GM}\right)\right]} & i\neq j \end{cases} \quad (47)$$

$$d_i(\gamma) = \sum_{r=-\frac{M}{2}}^{\frac{M}{2}-1} a_r\exp\left\{j\frac{2\pi}{GM}r\,[Gx - round(G\gamma) - Q + i - 1]\right\} = \frac{1}{2}\sum_{r=-\frac{M}{2}}^{\frac{M}{2}-1}\sum_{\rho=-\frac{1}{2},\frac{1}{2}}\exp\left\{j2\pi r\frac{[\rho + Gx - round(G\gamma) - Q + i - 1]}{GM}\right\} \quad (48)$$

c_q can then be calculated from Eq.(38) to Eq.(48). In the same manner, we can get d_p. Substituting $c_q(\gamma)$ and $d_p(\eta)$ into (32), we can get

$$I_{r,v} = \frac{1}{a_r b_v}\sum_{m=0}^{M-1}\sum_{n=0}^{N-1}B_{m,n}\sum_{q=-Q}^{Q}c_q(\gamma)\sum_{p=-Q}^{Q}d_p(\eta) \times\exp\left\{j\frac{2\pi}{GM}r\,[round\,(G\gamma)+q]\right\} \times\exp\left\{j\frac{2\pi}{GN}v\,[round\,(G\eta)+p]\right\} = \frac{1}{a_r b_v}\sum_{k=-\frac{GM}{2}}^{\frac{GM}{2}-1}\sum_{l=-\frac{GN}{2}}^{\frac{GN}{2}-1}\tilde{B}_{k,l}\exp\left(j\frac{2\pi}{GM}rk + j\frac{2\pi}{GN}vl\right) \quad (49)$$

where

$$\tilde{B}_{k,l} = \sum_m\sum_n B_{m,n}\left[c_{k-round(G\gamma_{m,n})}\left(\gamma_{m,n}\right) \cdot d_{l-round(G\eta_{m,n})}\left(\eta_{m,n}\right)\right] \quad (50)$$

From the above derivation, the process of the 2D NUFFT algorithm is as follows:

1) Calculate the interpolation coefficients $c_q(\gamma)$ and $d_p(\eta)$.
2) Calculate accurate factors a_r and b_v.
3) Calculate the interpolated new Fourier coefficient $\tilde{B}_{k,l}$.
4) Using 2D Inverse fast Fourier transform (IFFT) to calculate following equation

$$\tilde{I}_{r,v} = \sum_{k=-\frac{GM}{2}}^{\frac{GM}{2}-1}\sum_{l=-\frac{GN}{2}}^{\frac{GN}{2}-1}\tilde{B}_{k,l}\exp\left(j\frac{2\pi}{GM}rk + j\frac{2\pi}{GN}vl\right) \quad (51)$$

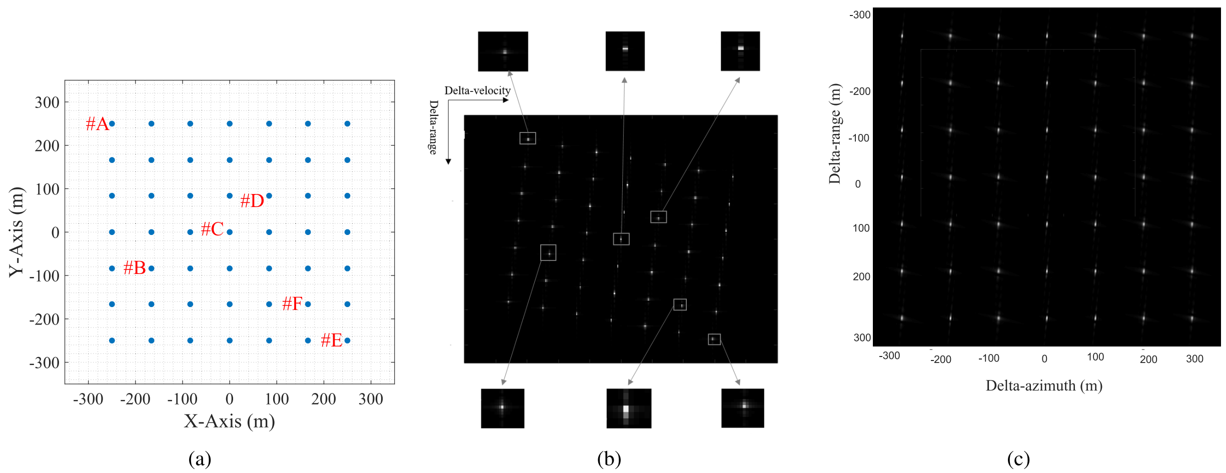

FIGURE 3. (a) 49-point target. (b) Imaged point-targets by the proposed algorithm. (c) Imagery of point target after SRGR conversion.

5) Using accurate factor a_r and b_v to scale the signal obtained in step 4).
6) Focusing image is obtained by the 2D-NUFFT.

B. SLANT RANGE TO GROUND RANGE CONVERSION

The range-velocity SAR image should be further converted to the ground plane image through slant range to ground range (SRGR) conversion. That is

$$\begin{aligned} I_{XY}(x,y) &= I_{RV}\left(r[x,y,0]^T, v[x,y,0]^T\right) \\ &= I_{RV}\left(k_0(\boldsymbol{s}) - \|\boldsymbol{P}_0\|_2, k_0(\boldsymbol{s}) - \frac{\langle \boldsymbol{P}_0, \boldsymbol{V}\rangle}{\|\boldsymbol{P}_0\|_2}\right) \end{aligned} \tag{52}$$

which can be implemented by a two-dimensional interpolation as follows

1) Take uniform pixels (x_l, y_l) in the X-Y plane, where $l = 1, 2, \ldots, L$.
2) $r\left([x_l, y_l, 0]^T\right)$ and $v\left([x_l, y_l, 0]^T\right)$ are calculated by (6), (7) and (24).
3) The non-uniform $I_{rv}\left(r[x,y,0]^T, v[x,y,0]^T\right)$ is interpolated into an image with a uniform range-velocity distribution. And we can get the corresponding X-Y plane image which distributed in range-azimuth domain.

V. PROCESSING RESULTS WITH SIMULATED AND EXPERIMENTAL DATA

To evaluate the effect of the acceleration model for highly squinted angle and the proposed 2D-NUFFT image processing algorithm, both experimental data and simulated results are provided in this section.

A. SIMULATION OF THE POINT TARGETS

Assuming that 49 point targets are evenly arrange in the scene of 600m × 600m. With considering the loss of windowing, the ideal range and azimuth resolution should be

$$\rho_r = c/2/B \times 0.886 \tag{53}$$

TABLE 1. Simulation parameters.

Parameters	Value	Symbol
Carrier frequency	14	GHz
Bandwidth	200	MHz
Sampling rate	240	MHz
Pulse width	5	μs
PRF	4.2	KHz
Acceleration vector	(-40, -26,24)	m/s^2
Velocity vector	(495 -734.24, 164)	m/s
Altitude	8	km
Squint angel	75	°

$$\rho_a = \frac{\lambda R_c}{2vT_s\cos^2\theta_s} \tag{54}$$

where B is the pulse bandwidth, λ represents the transmit signal wavelength. θ_s is the oblique viewing angle, R_c stands for the vertical range from the SAR platform to the target which located at scene center. the synthetic aperture time is T_s. v stands for the platform speed.

According to the relationship of Doppler resolution $\Delta f_d = \frac{2\Delta v}{\lambda}$ and the ideal velocity resolution $\Delta v = \frac{\lambda}{2T_s}$, we can get the ideal azimuth resolution through $\rho_a = \Delta v \frac{R_c}{v\cos^2\theta_s}$. Using the parameters listed in Table 1, we can get the $\rho_r = 0.6645$m, $\rho_a = 1.5648$m. So the resolution at the range and azimuth domain can also evaluate the performance of focusing imaging results.

We simulate 49-point targets in the imaging scene, as shown in Figure 3(a). Figure 3(b) is the imaging results of the 49 point targets. We randomly select six point-targets #A, #B, #C, #D, #E, #F, which can be correspond to the Figure 3(a) and give their enlarged focusing results to show imaging results more clearly. It must be noted that the target #C is the reference point. The two-dimensional side lobes are very clear and no coupling phenomenon from the Figure 3(b). Figure 3(c) is the imaging targets after the SRGR conversion, which is focusing image in range-azimuth domain. We analyze the range and azimuth dimension profiles for the three

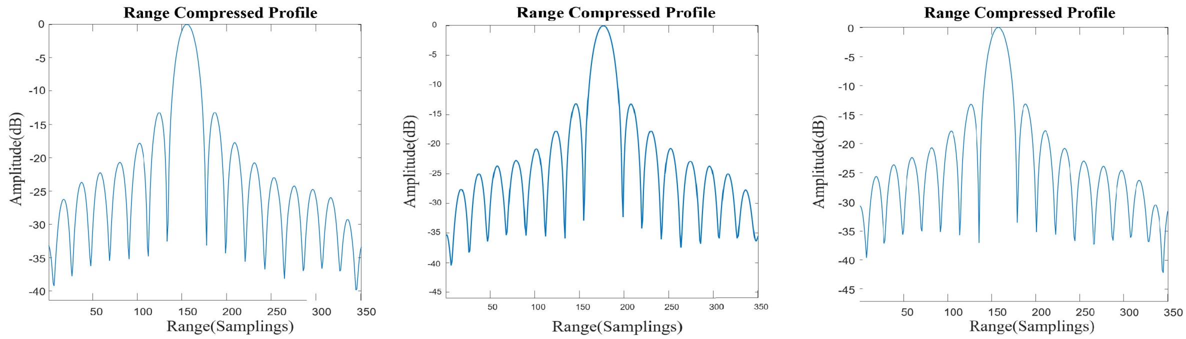

(a) (b) (c)

FIGURE 4. Range profile of three targets by 2D-NUFFT (a) Target #A (b) Target #C (c) Target #E.

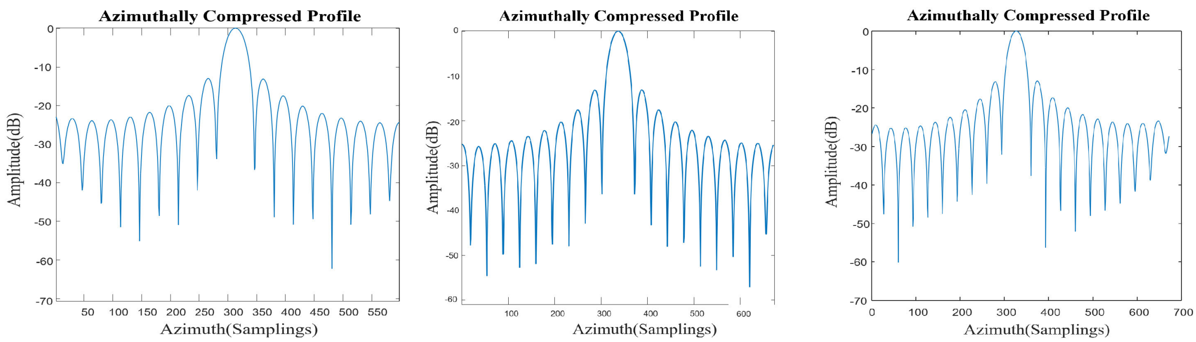

(a) (b) (c)

FIGURE 5. Azimuth profile of three targets by 2D-NUFFT. (a) Target #A. (b) Target #C. (c) Target #E.

TABLE 2. Image quality parameters of point targets.

Method	Position	Range			Azimuth		
		Resolution (m)	ISLR (dB)	PSLR (dB)	Resolution (m)	ISLR (dB)	PSLR (dB)
CA-Omega-K in [14]	Theoretical value	0.6645	-9.80	-13.26	1.5648	-9.80	-13.26
	Target #A	0.9205	-1.9488	-3.5134	3.3710	-1.9488	-3.5134
	Target #C	0.8636	-8.3499	-13.0292	2.7848	-8.7900	-12.3145
	Target #E	1.0356	-2.7851	-4.2086	3.5672	-2.6254	-1.6335
The proposed method	Target #A	0.7671	-9.8639	-13.2405	1.6046	-9.4736	-13.1985
	Target #C	0.7671	-9.8739	-13.2420	1.5648	-9.8815	-13.0375
	Target #E	0.7671	-9.8461	-13.2547	1.5913	-9.6538	-13.1938

point targets #A, #C and #E, as shown in Figure 4 and Figure 5, respectively. Those results indicates us that the side lobes are lower and the focusing effect is excellent.

B. COMPARISON WITH OTHER ALGORITHMS

We utilize the CA-Omega-K algorithm [14] to compare with the proposed algorithm. In this section, the specific parameters of number simulation set as Table 1.

Three common image indicators (resolution, peak sidelobe ratio(PSLR) and integration sidelobe ratio (ISLR)) are selected to evaluate imaging performance, as shown in Table 2. They are including range and azimuth domain. Then, three point targets (#A, #C and #E) are selected. The results of imaging performance are shown in Table 2.

At the same time, to highlight the effectiveness of our algorithm, Figure 6 and Figure 7 show the comparative impulse responses between our proposed algorithm and CA-Omega-K algorithm. We can conclude that:

1) The impulse responses of targets #A, #C and #E are well focused using the proposed algorithm;
2) The range resolution is the same as the theoretical value;
3) The azimuth resolution, ISLR and PSLR are close to the theoretical value.

However, the focusing results of targets using CA-Omega-K method does not achieve the desired results:

1) The reference target #C can get almost of the same focusing result with the proposed method;

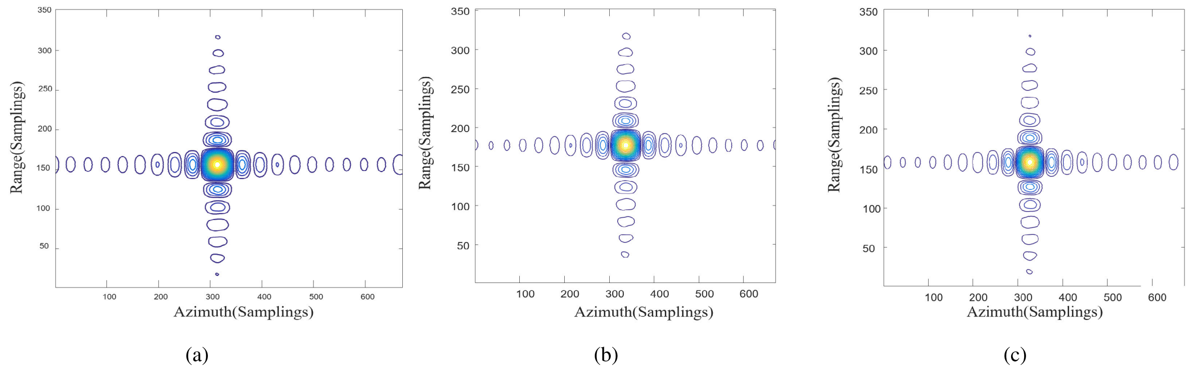

FIGURE 6. Focusing results of target by 2D-NUFFT. (a) Target #A. (b) Target #C. (c) Target #E.

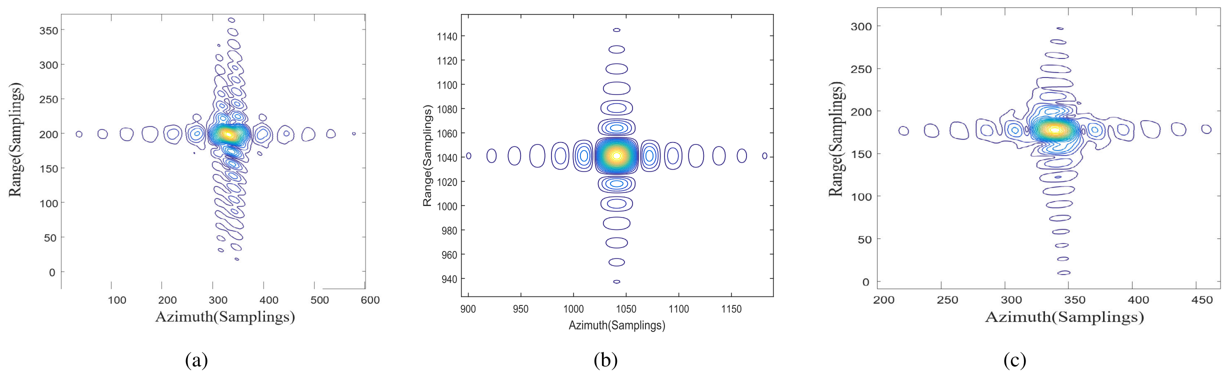

FIGURE 7. Focusing results of target_imaging by CA-Omega-K. (a) Target #A. (b) Target #C. (c) Target #E.

2) Point-targets of #A and #E at the edges in the range and azimuth direction can not focus properly;
3) The values of the three evaluation indicators (resolution, ISLR and PSLR) are much away from the theoretical value.

Since the CA-Omega-K algorithm just only suffices for small accelerations and velocity, its imaging results is poor. However, our proposed method satisfies the demands of the high-precision case for highly squinted SAR with large 3D acceleration.

C. FOCUSING IMAGE WITH EXPERIMENTAL DATA

We get the focusing image with the experimental data using the proposed method except the simulation of above-mentioned point-targets to explain the universality. Some specific simulation parameters are listed in Table 3. Figure 8 is focusing results of experimental data using 2D-NUFFT. Figure 8(a) and Figure 8(b) are the imaging results obtained by the proposed algorithm and imaging results after SRGR conversion, respectively. The 2D-NUFFT can obtain a well-focused squinted SAR image in the range-velocity domain. After SRGR correction, it still has perfect focusing effect.

To verify the focusing performance of the surface targets in the distributed scenarios, we select a strong target which marked by the red circle in the Figure 8(a) to evaluate the performance of scene imaging. With considering the loss of geometric correction, the ideal resolution of range is $\rho_r = c/2/B \times 0.886 = 0.886m$ using the bandwidth in the Table 3. Figure 9 shows the contour map, range profile and azimuth profile of the strong point. Also, the imaging performance of this strong point target is evaluated by spatial resolution, PSLR and ISIR, respectively as shown in the Table 4. From the the Table 4, we can derived that

TABLE 3. Simulation parameters of experimental data.

Parameters	Value	symbol
Carrier frequency	17	GHz
Bandwidth	150	MHz
Sampling rate	200	MHz
Pulse width	2	μs
PRF	12	KHz
Scene center coordinates	(1184, 0, 4731)	m
Squint angel	75	°

1) the resolution of range and azimuth domain of the strong point target imaging are close to the theoretical value;
2) Due to the influence of other point targets in the distributed scenarios, the theoretical value of the peak sidelobe comparison of the range dimension and the azimuth dimension are slightly increases.

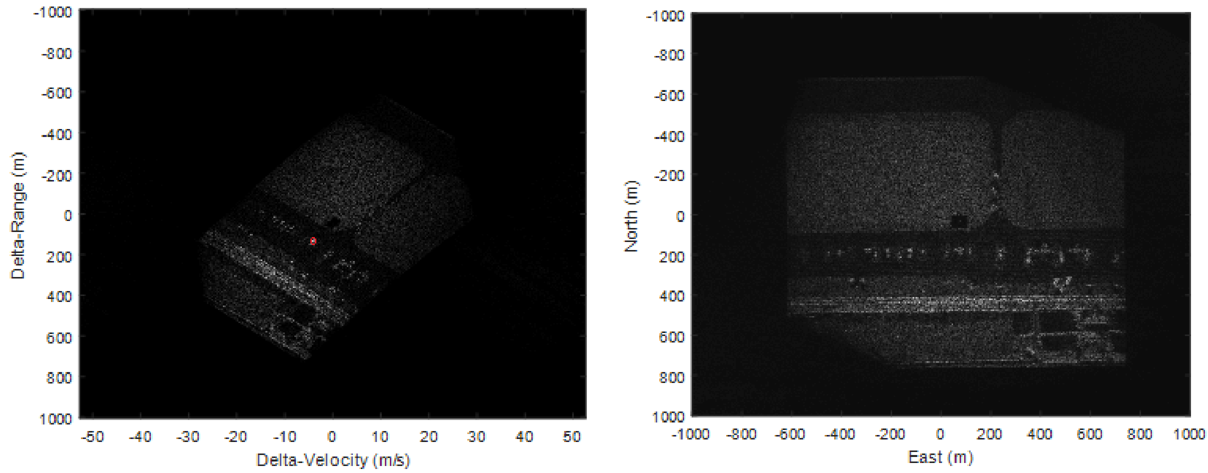

(a) (b)

FIGURE 8. Focusing results of scene_imaging by 2D-NUFFT. (a) Imaged scene by the algorithm. (b) Imagery of sence after SRGR.

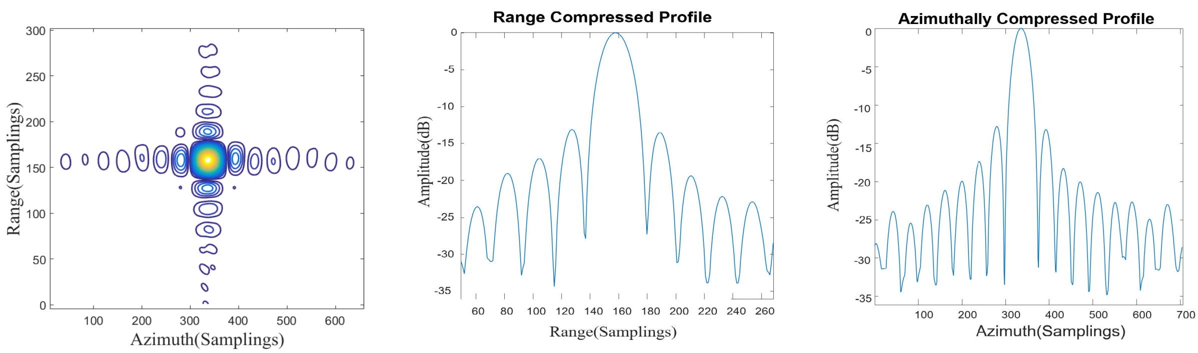

(a) (b) (c)

FIGURE 9. Focusing results of scene_imaging by 2D-NUFFT. (a) focusing resullt. (b) Range profile. (c) Azimuth profile.

TABLE 4. Image quality parameters of sence.

	Range			Azimuth		
	Resolution(m)	ISLR(dB)	PSLR(dB)	Resolution(m)	ISLR(dB)	PSLR(dB)
Theoretical value	0.886	-9.80	-13.26	1.4073	-9.80	-13.26
Actual value	0.912	-9.97	-13.06	1.4560	-9.74	-12.82

Those further validates the effectiveness of imaging algorithms based on 2D-NUFFT.

VI. CONCLUSION

In the case of high-resolution, highly squinted SAR imaging with three-dimensional acceleration, linear RCM produces a two-dimensional (2-D) spatial variable RCMs, which makes large squint SAR imaging has become difficult. However, most existing algorithms fail to consider these issues. In order to obtain high quality SAR images, this paper proposes a high precision 3D acceleration high squint SAR imaging processing algorithm.

In this paper, the method of Taylor expansion is used to get approximation of the three-dimensional acceleration large squint SAR range model. Next, the echo model is combined with the 2D-NUFFT algorithm which has already proposed in the field of mathematics to achieve image focusing. Compared with the traditional FFT, the main idea of the 2D-NUFFT algorithm is to use the nonlinear interpolation to complete the two-dimensional fast Fourier transform. This method not only solves the problem that the existing algorithm can not focus on the SAR image in the case of nonlinear flight trajectory, but also further reduces the calculation cost.

In order to make the SAR echo signal processed by the algorithm easier to achieve terrain matching, this paper introduces the SRGR algorithm in detail on the basis of the existing. Finally, this paper evaluates the imaging effects of multiple point targets and simulated scenes by evaluating three common indicators (i.e. PSLR, ISLR and resolution) among the six indicators of SAR images. The results of the evaluation verify the effectiveness of the proposed algorithm in three-dimensional accelerated squint SAR in high-precision imaging. Compared with the CA-Omega-K algorithm [14] algorithm, the proposed algorithm has better robustness.

One of the innovation of this paper is to apply the existing 2D-NUFFT algorithm in the field of mathematics to SAR image processing. The superiority of the 2D-NUFFT algorithm makes the process of high-precision three-dimensional acceleration large squint SAR imaging processing simpler and more efficient. The second is to introduce the principle and implementation of the SRGR in further detail. However, it has to be proposed that the algorithm in this paper is only a satisfactory result in the simulation, and the next step will continue to improve the algorithm to achieve its industrialization goal.

ACKNOWLEDGMENTS

The authors would like to thank the editors and the anonymous reviewers for their constructive comments that significantly improved the quality of this paper.

REFERENCES

[1] D. Li, G. Liao, W. Wang, and Q. Xu, "Extended azimuth nonlinear chirp scaling algorithm for bistatic SAR processing in high-resolution highly squinted mode," *IEEE Geosci. Remote Sens. Lett.*, vol. 11, no. 6, pp. 1134–1138, Jun. 2014.

[2] H. Zhong and X. Liu, "An extended nonlinear chirp-scaling algorithm for focusing large-baseline azimuth-invariant bistatic SAR data," *IEEE Geosci. Remote Sens. Lett.*, vol. 6, no. 3, pp. 548–552, Jul. 2009.

[3] X. Qiu, C. Li, J. Li, X. Zhao, and Y. Wang, "A CZT-based continuous varying PRF polar format algorithm for highly squinted spotlight SAR," in *Proc. IEEE Int. Geosci. Remote Sens. Symp. (IGARSS)*, Milan, Italy, Jul. 2015, pp. 4494–4497.

[4] X. Nie, S. Shen, G. Guo, and L. Zhuang, "A beam segmentation based 2-step polar format algorithm for highly squinted SAR," in *Proc. IEEE Radar Conf. (RadarConf)*, Oklahoma City, OK, USA, Apr. 2018, pp. 1472–1475.

[5] L. Gaogao, P. Li, S. Tang, and L. Zhang, "Focusing highly squinted data with motion errors based on modified non-linear chirp scaling," *IET Radar, Sonar Navigat.*, vol. 7, no. 5, pp. 568–578, Jun. 2013.

[6] P. Chen and J. Kiang, "An improved range-doppler algorithm for SAR imaging at high squint angles," *Progr. Electromagn. Res.*, vol. 53, pp. 41–52, Jan. 2017.

[7] M. Xing, X. Jiang, R. Wu, F. Zhou, and Z. Bao, "Motion compensation for UAV SAR based on raw radar data," *IEEE Trans. Geosci. Remote Sens.*, vol. 47, no. 8, pp. 2870–2883, Aug. 2009.

[8] J. Lu, L. Zhang, P. Xie, Z. Meng, and Y. Cao, "High-resolution imaging of multi-channel forward-looking synthetic aperture radar under curve trajectory," *IEEE Access*, vol. 7, pp. 51211–51221, 2019.

[9] J. Liu, X. Qiu, L. Huang, and C. Ding, "Curved-path SAR geolocation error analysis based on BP algorithm," *IEEE Access*, vol. 7, pp. 20337–20345, 2019.

[10] Y. Liu, W. Wang, X. Pan, Q. Fu, and G. Wang, "Inverse omega-K algorithm for the electromagnetic deception of synthetic aperture radar," *IEEE J. Sel. Topics Appl. Earth Observ. Remote Sens.*, vol. 9, no. 7, pp. 3037–3049, Jul. 2016.

[11] Z. Xiao, "A modified wave-number domain algorithm for missile-borne squinted SAR data processing," *J. Electron. Inf. Technol.*, vol. 33, pp. 1453–1458, 2011.

[12] T. Xiong, M. Xing, X.-G. Xia, and Z. Bao, "New applications of omega-K algorithm for SAR data processing using effective wavelength at high squint," *IEEE Trans. Geosci. Remote Sens.*, vol. 51, no. 5, pp. 3156–3169, May 2013.

[13] X. Qiu, D. Hu, and C. Ding, "An omega-K algorithm with phase error compensation for bistatic SAR of a translational invariant case," *IEEE Trans. Geosci. Remote Sens.*, vol. 46, no. 8, pp. 2224–2232, Aug. 2008.

[14] S. Tang, L. Zhang, P. Guo, and Y. Zhao, "An omega-K algorithm for highly squinted missile-borne SAR with constant acceleration," *IEEE Geosci. Remote Sens. Lett.*, vol. 11, no. 9, pp. 1569–1573, Sep. 2014.

[15] S. Tang, L. Zhang, P. Guo, G. Liu, and G. C. Sun, "Acceleration model analyses and imaging algorithm for highly squinted airborne spotlight-mode SAR with maneuvers," *IEEE J. Sel. Topics Appl. Earth Observ. Remote Sens.*, vol. 8, no. 3, pp. 1120–1131, Mar. 2015.

[16] S.-X. Zhang, M.-D. Xing, X.-G. Xia, L. Zhang, R. Guo, and Z. Bao, "Focus improvement of high-squint SAR based on azimuth dependence of quadratic range cell migration correction," *IEEE Geosci. Remote Sens. Lett.*, vol. 10, no. 1, pp. 150–154, Jan. 2013.

[17] G. Sun, X. Jiang, M. Xing, Z.-J. Qiao, Y. Wu, and Z. Bao, "Focus improvement of highly squinted data based on azimuth nonlinear scaling," *IEEE Trans. Geosci. Remote Sens.*, vol. 49, no. 6, pp. 2308–2322, Jun. 2011.

[18] D. Li, H. Lin, H. Liu, G. Liao, and X. Tan, "Focus improvement for high-resolution highly squinted SAR imaging based on 2-D spatial-variant linear and quadratic RCMs correction and azimuth-dependent Doppler equalization," *IEEE J. Sel. Topics Appl. Earth Observ. Remote Sens.*, vol. 10, no. 1, pp. 168–183, Jan. 2017.

[19] Y. Kong, B. Cho, and Y. Kim, "Ambiguity-free Doppler centroid estimation technique for airborne SAR using the radon transform," *IEEE Trans. Geosci. Remote Sens.*, vol. 43, no. 4, pp. 715–721, Apr. 2005.

[20] Y. Dang, Y. Liang, B. Bie, J. Ding, and Y. Zhang, "A range perturbation approach for correcting spatially variant range envelope in diving highly squinted SAR with nonlinear trajectory," *IEEE Geosci. Remote Sens. Lett.*, vol. 15, no. 6, pp. 858–862, Jun. 2018.

[21] O. M. Bucci and M. D. Migliore, "A novel nonuniform fast Fourier transform algorithm and its application to aperiodic arrays," *IEEE Antennas Wireless Propag. Lett.*, vol. 16, pp. 1472–1475, 2017.

[22] X. Zhou, H. Sun, J. He, and X. Lu, "NUFFT-based iterative reconstruction algorithm for synthetic aperture imaging radiometers," *IEEE Geosci. Remote Sens. Lett.*, vol. 6, no. 2, pp. 273–276, Apr. 2009.

[23] J. Song, Q. H. Liu, P. Torrione, and L. Collins, "Two-dimensional and three-dimensional NUFFT migration method for landmine detection using ground-penetrating radar," *IEEE Trans. Geosci. Remote Sens.*, vol. 44, no. 6, pp. 1462–1469, Jun. 2006.

[24] Y. L. Neo, F. Wong, and I. G. Cumming, "A two-dimensional spectrum for bistatic SAR processing using series reversion," *IEEE Geosci. Remote Sens. Lett.*, vol. 4, no. 1, pp. 93–96, Jan. 2007.

[25] B. Liu, Y. Wang, and S. Han, "A real-time associative algorithm of RCMC and SRGR," *J. Electron. Inf. Technol.*, vol. 31, no. 5, pp. 1099–1102, May 2009.

[26] B. Huang, X. Zhao, D. Du, S. Zhang, and W.-Q. Wang, "Highly squinted imaging for diving SAR with 3-dacceleration," in *Proc. IEEE Int. Geosci. Remote Sens. Symp.*, Valencia, Spain, Jul. 2018, pp. 8917–8920.

[27] J. Song, Y. Liu, S. L. Gewalt, G. Cofer, G. A. Johnson, and Q. H. Liu, "Least-square NUFFT methods applied to 2-D and 3-D radially encoded MR image reconstruction," *IEEE Trans. Biomed. Eng.*, vol. 56, no. 4, pp. 1134–1142, Apr. 2009.

[28] S. Zhao, R. Wang, Y. Deng, Z. Zhang, N. Li, L. Guo, and W. Wang, "Modifications on multichannel reconstruction algorithm for SAR processing based on periodic nonuniform sampling theory and nonuniform fast Fourier transform," *IEEE J. Sel. Topics Appl. Earth Observ. Remote Sens.*, vol. 8, no. 11, pp. 4998–5006, Nov. 2015.

[29] B. Fan, J. Wang, Y. Qin, H. Wang, and H. Xiao, "Polar format algorithm based on fast Gaussian grid non-uniform fast Fourier transform for spotlight synthetic aperture radar imaging," *IET Radar, Sonar Navigat.*, vol. 8, no. 5, pp. 513–524, Jun. 2014.

[30] S. Zhang and C. Liu, "Two-dimensional non-uniform FFT for image formation of high-squint SAR," *IEEE Geosci. Remote Sens. Symp.*, Quebec City, QC, Canada, Jul. 2014, pp. 644–647.

[31] J. F. White, "Matrix analysis," in *High Frequency Techniques: An Introduction to RF and Microwave Design and Computer Simulation*. Piscataway, NJ, USA: IEEE, 2004.

BANG HUANG was born in Hubei, China, in 1994. He received the B.E. degree from the School of Communication and Information Engineering, Chongqing University of Posts and Telecommunications, Chongqing, China, in 2017. He is currently pursuing the M.E. degree in electronic and communication engineering with the University of Electronic Science and Technology of China (UESTC), Chengdu, China.

His research interests include SAR imaging of high-precision and SAR jamming using frequency diverse array (FDA).

SHUNSHENG ZHANG was born in Anhui, China, in 1980. He received the Ph.D. degree in signal and information processing from the Beijing Institute of Technology, Beijing, China, in 2007. In October 2007, he joined the Research Institute of Electronic Science and Technology, University of Electronic Science and Technology of China, Chengdu, China, where he became an Associate Professor, in August 2009. From May 2014 to May 2015, he was a Visiting Scholar with the Department of Electrical and Computer Engineering, National University of Singapore. His major research interests include radar imaging (SAR/ISAR) and the application of frequency diverse array technology.

WEN-QIN WANG (M'08–SM'16) received the B.E. degree in electrical engineering from Shandong University, Shandong, China, in 2002, and the M.E. and Ph.D. degrees in information and communication engineering from the University of Electronic Science and Technology of China (UESTC), Chengdu, China, in 2005 and 2010, respectively. From March 2005 to 2007, he was with the National Key Laboratory of Microwave Imaging Technology, Chinese Academy of Sciences, Beijing, China. From June 2011 to May 2012, he was a Visiting Scholar with the Stevens Institute of Technology, Hoboken, NJ, USA. From December 2012 to December 2013, he was a Hong Kong Scholar with the City University of Hong Kong, Hong Kong. From January 2014 to January 2016, he was a Marie Curie Fellow with Imperial College London, U.K. Since September 2007, he has been with the School of Information and Communication Engineering, UESTC, where he is currently a Professor and the Director. His research interests include array signal processing and circuit systems for radar, communications, and microwave remote sensing.

TIANXING LIAO received the B.E. degree in communication engineering from the South-Central University for Nationalities (SCUN), Wuhan, China, in 2015. He is currently pursuing the Ph.D. degree with the School of Information and Communication Engineering, University of Electronic Science and Technology of China (UESTC), Chengdu, China. His research interests include array processing and graph signal processing.

XIN ZHAO was born in August 1978. She received the B.E. degree from Communication Engineering, Sichuan University, Sichuan, China, and the M.E. degree in communication and electronic engineering from the Graduate School, Chinese Academy of Sciences (CAS), Beijing, China. She is currently a Researcher with the Beijing Institute of Mechanical and Electrical Engineering. She has published 11 national defense patents. Her major research interests include the target characteristics and radar signal processing. She received a third prize of national defense science and technology progress.

DUNWEI DU was born in August 1988. He received the master's degree from the Beijing Institute of Technology, in 2013. He is currently an Engineer with the Beijing Electromechanical Engineering Institute. His areas of expertise are overall design technology for seeker, target characteristic, radar signal processing, and experimental verification. He took part in the writings of Battlefield electromagnetic environment simulation and experimental identification technology of air defense missiles.